



HAL
open science

An in-situ experimental HP/HT study on bromine release from a natural basalt

Tobias Grützner, H el ene Bureau, Eglantine Boulard, Pascal Munsch, Nicolas Guignot, Julien Siebert, Yoann Guarnelli

► **To cite this version:**

Tobias Gr utzner, H el ene Bureau, Eglantine Boulard, Pascal Munsch, Nicolas Guignot, et al.. An in-situ experimental HP/HT study on bromine release from a natural basalt. *Chemical Geology*, 2024, 644, pp.121869. <10.1016/j.chemgeo.2023.121869>. <hal-04338237>

HAL Id: hal-04338237

<https://hal.science/hal-04338237v1>

Submitted on 12 Dec 2023

HAL is a multi-disciplinary open access archive for the deposit and dissemination of scientific research documents, whether they are published or not. The documents may come from teaching and research institutions in France or abroad, or from public or private research centers.

L'archive ouverte pluridisciplinaire **HAL**, est destin ee au d ep ot et  a la diffusion de documents scientifiques de niveau recherche, publi es ou non,  emanant des  tablissements d'enseignement et de recherche fran ais ou  trangers, des laboratoires publics ou priv es.



HAL Authorization

1 An in-situ experimental HP/HT study on bromine release from a
2 natural basalt

3

4 Tobias Grützner^{1,2,3*}, Hélène Bureau¹, Eglantine Boulard¹, Pascal Munsch⁴, Nicolas
5 Guignot⁵, Julien Siebert⁶, Yoann Guarnelli¹

6

7 ¹ Institut de Minéralogie, de Physique des Matériaux et de Cosmochimie (IMPMC),
8 Sorbonne Université, CNRS UMR 7590, 75252 Paris Cedex 05, France.

9 ² Research School of Earth Sciences, Australian National University, Canberra,
10 Australia.

11 ^{3*}Institut für Geowissenschaften, Goethe-Universität Frankfurt, Germany.

12 ⁴ Institut de Recherche en Astrophysique et Planétologie (IRAP), Toulouse, France.

13 ⁵ Synchrotron SOLEIL, Saint-Aubin France.

14 ⁶ Institut de physique du globe de Paris, France

15

16 *Corresponding author and present address.

17

18 Email addresses: tobias.gruetzner@wwu.de (T. Grützner), helene.bureau@upmc.fr (H.
19 Bureau), eglantine.boulard@sorbonne-universite.fr (E. Boulard),
20 pascal.munsch@irap.omp.eu (P. Munsch), nicolas.guignot@synchrotron-soleil.fr (N.

21 Guignot), siebert@ipgp.fr (J. Siebert); yoann.guarnelli@sorbonne-universite.fr (Y.

22 Guarnelli).

23

24 ABSTRACT

25 We present the first in-situ partitioning data for bromine between a natural basaltic melt
26 and a coexisting fluid. For this study hydrothermal diamond anvil cell experiments at
27 pressures up to 1.7 GPa were conducted. We combined laser heating to melt the basalt
28 glass with external heating to lower the temperature gradient in the cell and to initiate
29 circulation for the aqueous fluid. Bromine concentrations were measured in-situ with X-
30 ray fluorescence in the basaltic melts, glasses, and in the fluid. From the results we
31 calculated partition coefficients of $D^{\text{Br}}_{\text{fluid/melt}} = 1.19$ to 3.92 in the range of 0.4 to 1 GPa
32 for aqueous fluids. Experiments with neon as the surrounding fluid ($D^{\text{Br}}_{\text{fluid/melt}} = 0.38 \pm$
33 0.01 at 1.1 GPa) suggest that Br-release from a basalt into volatiles that have no
34 bonding affinity with Br is weak. This should be the case for dry intra-plate volcanic
35 eruptions. From the experimentally gained partition coefficients and from global Br
36 concentration values in melt inclusions of arc magmas, we calculated an annual global
37 Br flux of $23.5 - 72.9 \times 10^9$ g/y.

38

39 KEYWORDS

40 bromine, fluid/melt partitioning, volcanic degassing, SXRF, hydrothermal diamond anvil

41 cell

42

43 1. INTRODUCTION

44 Halogens are very reactive chemicals and play a significant role as volatile elements in
45 geodynamic processes. In crustal hydrothermal fluids (e.g., brines and molten salts),
46 halogens are major agents for the metal transport and thus play a critical role in ore-
47 forming processes (Aiuppa et al., 2009). Halogens are also important constituents of
48 volcanic fumaroles and volcanic ejecta. Once released to the atmosphere halogens
49 have an environmental impact and can e.g., contribute to ozone destruction (e.g.,
50 Daniel et al., 1999; Gerlach et al., 2004).

51 The heavy halogen bromine (Br) has a low abundance on Earth, but it is highly reactive
52 and an important chemical agent in the atmosphere (Fehn, 2012). Besides plankton and
53 burning biomass, volcanoes have been recognized as a significant (Gerlach et al.,
54 2004) if not the controlling, (Pyle and Mather, 2009) contributor to the actual
55 atmospheric Br content. Especially arc volcanoes release large amounts of Br gas
56 compounds: The first detection of volcanic BrO has been recorded by Bobrowski et al.
57 (2003) from the Soufrière Hills volcano (Montserrat). Since then, Br gas compounds
58 have been reported in several case studies e.g., from Mt. Etna (Aiuppa et al., 2005;
59 Pyle and Mather, 2009; Bobrowski and Giuffrida, 2012; Roberts et al. 2018) or Mt.
60 Masaya (Witt et al, 2008).

61 Based on models from Etna's degassing measurements Br is estimated to be rather
62 less abundant in basalts compared to e.g., chlorine (Cl) or sulfur (Bobrowski and
63 Giuffrida, 2012). The Br concentrations range from $\mu\text{g/g}$ to ng/g in volcanic rocks and in
64 mantle rocks (Newsom, 1995). Yet, Br fluxes from arc volcanoes are estimated to be in
65 the range of $5\text{-}15 \times 10^9$ g/y HBr per year (Aiuppa et al., 2005; Pyle and Mather, 2009,

66 Webster et al., 2018, Cadoux et al., 2022). HBr is the dominant species of Br emitted
67 from volcanoes (Roberts et al., 2018). Once in the stratosphere, Br is notably involved
68 in the destruction of ozone as it reacts to form BrO and eventually BrO_x (Bobrowski et
69 al., 2003). These conversions are significant: 1 ng/g of BrO can destroy about 10 ng/g
70 of ozone per minute (Bobrowski et al., 2003). This is about 60 times more efficient
71 (Sinnhuber et al., 2009) than the ozone destruction by Cl in this respect (Daniel et al.,
72 1999; Gerlach et al., 2004; Gutmann et al., 2018 for review).

73 However, the deep cycling of Br, its behavior in magmas, and the transfer to the Earth's
74 surface is poorly understood. There is scant data, but Br solubility has been shown to
75 be very high in silica-rich systems (Bureau and Métrich, 2003; Bureau et al., 2010).
76 Depending on the Br content in degassing magmas the annual volcanological Br flux to
77 the atmosphere could be strongly underestimated, and therefore, the impact of Br on
78 ozone destruction in the Earth's stratosphere as well.

79 So far, there are only a few experimental studies about Br partitioning between a silicate
80 melt and a fluid. The pioneering study was conducted by Bureau et al. (2000) with an
81 albitic melt composition at 200 MPa from which the authors calculated a partition
82 coefficient between the aqueous fluid and the silicate melt of $D_{\text{fluid/melt}}^{\text{Br}} = 17.5 \pm 0.6$.
83 Bureau et al. (2010) found smaller values with $D_{\text{fluid/melt}}^{\text{Br}}$ ranging from 2.18 to 9.2 ± 0.5
84 between aqueous fluids/saline fluids and a haplogranitic melt at higher pressures of
85 0.66 to 1.7 GPa. Using a similar haplogranitic melt, Louvel et al. (2020b) found values of
86 $D_{\text{fluid/melt}}^{\text{Br}}$ between 2.0 ± 0.2 and 15.3 ± 2.0 at pressures of 0.2 to 1.7 GPa. Louvel and
87 coworkers did not find a clear correlation with pressure or temperature in their results.
88 The experiments from Bureau et al. (2010) and Louvel et al. (2020b) were measured in-

89 situ and give a good insight into Br partitioning between melt and fluid, but they were
90 conducted in compositionally simplified systems (e.g., Fe-free melts) and rather aimed
91 to study more evolved melts like sediment melt composition with higher SiO₂ content.

92 Cadoux et al. (2018) conducted partitioning experiments for Br between fluid and a
93 wider range of arc-related rocks: natural basalt, andesite, and rhyodacite at 100-200
94 MPa. They calculated $D_{\text{fluid/melt}}^{\text{Br}}$ of 4.6 to 27.9 with basalt at the lower end and
95 rhyodacite at the upper end of their partition coefficients. Experiments from Cadoux et
96 al. (2018) show generally higher partition coefficients than the results from Bureau et al.
97 (2010) which could describe the impact of the lower pressure used by Cadoux et al.
98 (2018).

99 Not much is known about the effect of the different cations on $D_{\text{fluid/melt}}^{\text{Br}}$. Bromine
100 concentrations vary in water-saturated silicic melts with (Na+K)/Al molar ratio and reach
101 a minimum at (Na+K)/Al = 1 (Bureau and Métrich, 2003). A comparison to Cl advocates
102 for the presence of alkalis to increase Br solubility: Cl solubility in melts is controlled by
103 the abundances of several elements like Mg, Ca, Fe, Na, K, Al, Li, Rb, Cs, Ti, F, and P
104 (Webster and de Vivo, 2002; Webster et al., 1999). Cochain et al. (2015) demonstrate
105 that alkalis and especially Na can retain Br in a silicate melt while it degasses more
106 efficiently from hydrous melts. Louvel et al. (2020b) find that Br prefers Na over OH in
107 silicate glasses, where it is incorporated in a salt-like structure, like NaBr. Louvel et al.
108 (2020a) show that Br bonds with network modifiers in granitic melts but does not find
109 any affinity to prefer Na⁺ over e.g., K⁺ or Ca²⁺ if all three are present.

110 In this study we present new Br degassing experiments from a natural arc-related basalt
111 into an aqueous fluid and into neon. The experiments were conducted over a pressure

112 range from 0.4 to 1.7 GPa in the closed system of a diamond anvil cell which has
113 already been used successfully by Bureau et al. (2010), to study Br. Partitioning of Br
114 between the basalt and the surrounding fluid can be calculated from both in-situ
115 measurements on melts and on quenched glass.

116

117 2. METHODS

118 2.1. Diamond anvil cell setup

119 Two series of experiments were performed as hydrous and neon experiments which
120 refer to the pressure media water and neon, respectively. As the basalt glass with about
121 2 wt.% of water was also used in the *neon* runs, these runs were not completely dry
122 *sensu stricto* (for a detailed description of the starting material see further below). The
123 water-basalt-partitioning experiments (hydrous) were conducted in externally heated
124 hydrothermal diamond anvil cells (HDAC) of either the Basset type (e.g., Basset, 2003)
125 or a modified Basset type with pressure-driving membranes (Munsch et al., 2015).
126 Similar setups have been used successfully in former studies on heavy halogen
127 behavior in silicate glass and hydrothermal fluids (e.g., Bureau et al., 2010, 2016;
128 Louvel et al., 2020b). All HDAC are equipped with 2 mm thick diamonds with large
129 culets of 1 mm diameter. The sample chamber is compressed between two diamonds
130 and has a diameter of 500 μm which is drilled as a hole into a Re gasket of either 100
131 μm or 200 μm initial thickness. The aqueous fluid serves as a pressure medium within
132 the sample chamber. Both diamonds are mounted on tungsten carbide (WC) seats. A
133 molybdenum wire coiled around each WC seat serves as external heater. The

134 temperature can be measured with K-type thermocouples that are glued with cement to
135 each of the diamond anvils. The temperature offset between the thermocouple position
136 and the sample chamber has been calibrated at ambient pressure against the melting
137 temperature of pure sulfur (112.8 °C), NaNO₃ (308 °C), CsCl (645 °C), and NaCl (801
138 °C). To avoid oxidation of the diamonds while using the external heaters, the HDAC are
139 connected to a gas supply system and can be flooded with a reducing gas mix like Ar-
140 H₂ (4 vol.%).

141 For neon experiments we used an inert gas as pressure medium. We performed neon-
142 basalt partitioning experiments which were conducted in modified Chervin-type diamond
143 anvil cells (Chervin et al., 1995). These DAC are equipped with a pressure driving
144 membrane like the Basset-type HDAC but do not have an external heating system.
145 Chervin type cells (CDAC) can be installed into the gas loading system e.g., at the
146 Institut de Minéralogie, de Physique des Matériaux et de Cosmochimie (IMPMC –
147 Sorbonne Université Paris) where we loaded the sample chamber with neon gas
148 instead of water as a pressure medium (Couzinet et al., 2003). Neon has a density like
149 air. It was loaded with an initial pressure of about 0.5 GPa into the DAC. At this
150 pressure neon behaves as a (supercritical) fluid. The CDAC are equipped with the same
151 type of diamonds, rhenium gaskets, and the same sample chamber dimensions that
152 were used for the HDAC. All used DAC types in this study allow observation of the
153 experiment and laser heating along the pressure axis through the diamond anvils.

154

155 2.2. Experimental runs, heating, and temperature determination

156 For each experiment the sample chambers were filled with 1-3 larger pieces of basalt
157 glass (about 30-50 vol.%, 55-75 wt.% respectively), and 50-70 vol.% of either water or
158 neon gas (+ small flakes of gold + ruby spheres in neon experiments for pressure
159 determination). The samples were compressed to about 1-2 GPa before the run. To
160 heat the basalt glass to its liquid state, we used two YAG laser that can be focused on
161 the sample from both sides of the pressure axis – one through each diamond. YAG
162 laser can be used as the iron content of the basalt glass starting material (8.45 wt.%) is
163 high enough to provide the required absorption. During the heating the melt was
164 analyzed with Synchrotron X-Ray Diffraction (SXRD) to test for the presence of crystals
165 in the melt. If crystals (olivine or pyroxene) were present, the laser temperature was
166 increased stepwise until all the crystals were melted. The laser heating temperature
167 ranged from 1725 to 2167 °C for the neon experiments. It could not be measured for
168 hydrous experiments but by monitoring the absence of crystals by XRD we could
169 ensure to stay above the liquidus. This would be a temperature of 1300 to 1400 °C for
170 the hydrous basalt. Experimental conditions are listed in Table 1.

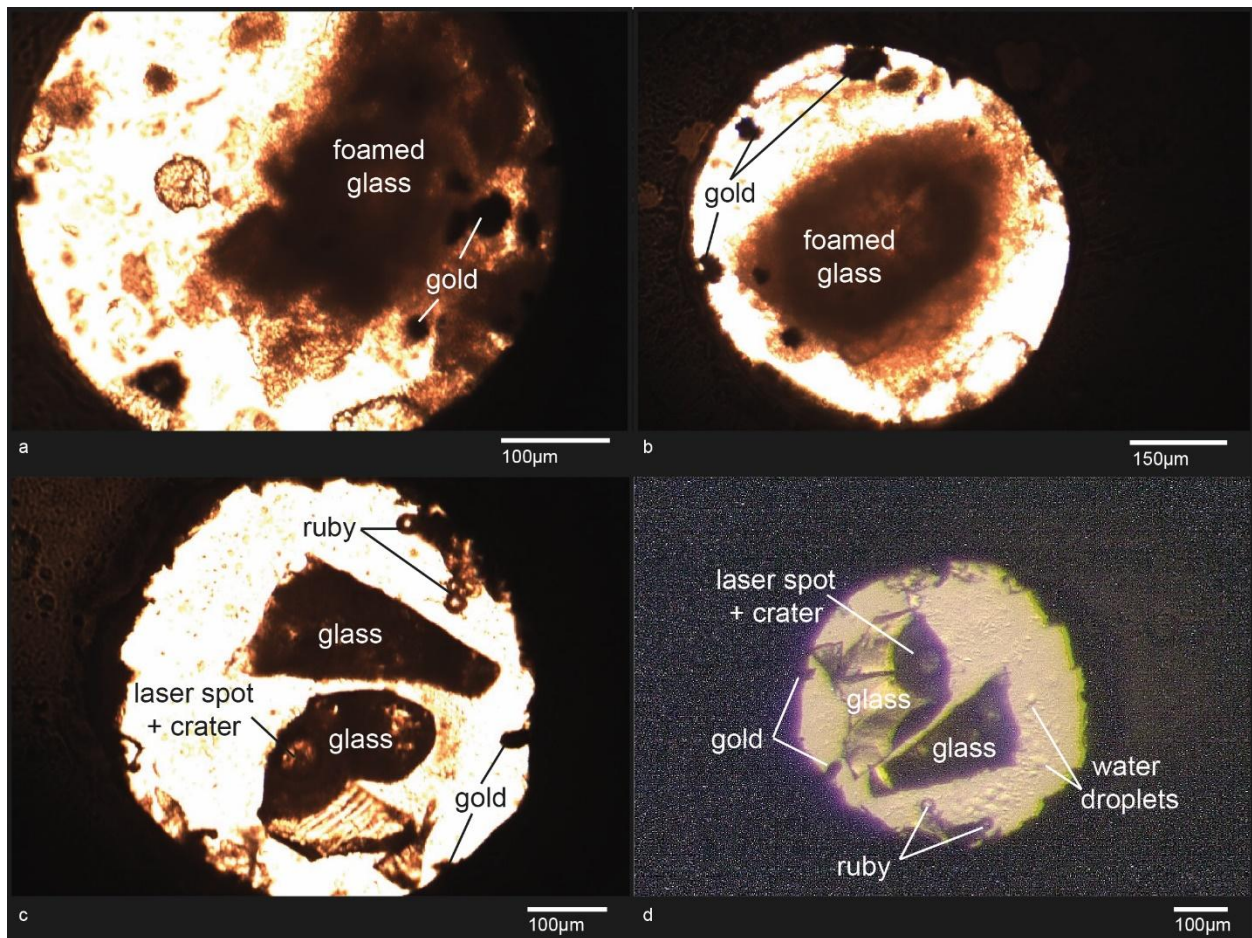
171 For the hydrous experiments heating cycles (usually 5 min at the peak temperature) and
172 decompression paths were varied between each run: During experiment LN11 and
173 LN22 the basalt glass was heated with the laser to its liquid state and quenched
174 afterwards by shutting off the laser. Br concentrations were then analyzed in the glass
175 and in the fluid. This heating-quenching-analyzing cycle was repeated several times
176 with a stepwise pressure release in the sample chamber after each cycle to test for
177 pressure effects on Br partitioning (c.f. Bureau et al., 2010, 2016; Leroy et al., 2019) and
178 to reach chemical equilibrium (see further below in the Results section for detailed

179 description). Experiment Cpo2 had only one heating-quenching cycle. For experiment
180 Cpo3 the laser heating was not switched off for the decompression steps, but instead it
181 was constantly keeping the basalt above the liquidus. The Br concentration was
182 analyzed in the fluid of Cpo3 while the laser was switched on and the basalt was still
183 molten. During run Cpo2, Cpo3 and LN22 the external heaters were additionally heating
184 the sample chamber of the HDAC for the entire run (244 °C, 265 °C and 235 °C
185 respectively). This minimized the temperature gradient caused by the heating laser and
186 induced a better circulation and homogenization of the fluid. To test this effect the
187 external heating system was shut off in experiment LN11: the fluid was not heated
188 externally, and Br was measured at two fixed positions (Figure 1a): The first spot is next
189 to the melted and quenched basalt. The second spot is about 200-300 μm away at the
190 rim of the sample chamber (as it was also the case for all other hydrous experiments).
191 During the laser heating the temperature of the HDAC measured at the thermocouples
192 increased to 260 – 280 °C. This was independent from the external heating system
193 being switched on (LN22, Cpo3) or off (LN11).

194 The neon experiments Hak1 and Hak2 were performed in CDAC with neon as the
195 pressure medium and with similar heating cycles as described above for LN11 and
196 LN22: after crossing the basalt glass transition with the laser and keeping the laser for 5
197 min at the peak temperature, the laser was shut off, Br concentrations were analyzed in
198 the glass and in the fluid (neon), and the pressure was decreased before starting the
199 next heating cycle again. During the experiment of Hak1 Br was additionally measured
200 twice in the basaltic melt during each heating cycles. After the conduction of run Hak1
201 the cell was kept closed and directly re-compressed to 1.4 GPa to conduct run Hak2 on

202 the same loading. Mar1 had only one long heating cycle: The laser was not switched off
203 during the decompression steps and for each decompression step in Mar1 Br
204 concentration was measured in the liquid basalt (600 sec. for each analysis).

205



206
207 Figure 1 Optical microscope images of sample chambers and experimental
208 samples LN11, LN22, Hak2 and Hak1. a) LN11: Two spots of measurement for the
209 aqueous fluid were chosen. One close to the melted glass and one as far away as
210 possible within the sample chamber. b) LN22: like in a) the basalt glass shows a foam-
211 like texture after treatment with the heating laser. c) Hak2: In contrast to a) and b) laser
212 heated glass in coexistence with neon retains its glassy texture. d) Hak1: During heating

213 cycle 3 and ongoing decompression of the cell water droplets could be observed in the
214 sample chamber.

215

216

217 2.3. Pressure determination

218 2.3.1. Setup

219 Pressure determination in the loaded and compressed DAC was conducted in several
220 ways using (1) ruby fluorescence, (2) gold SXR, and the (3) water-ice phase transition.

221 (1) For the neon experiments small ruby spheres were added during loading into the
222 sample chamber of the CDAC. The pressure was measured at room temperature before
223 and after the run with the fluorescence method at the IMPMC and at Soleil. The
224 fluorescence wavelength shift of ruby is a commonly used pressure sensor for DAC
225 experiments (e.g., Chervin et al., 2001; Shen et al., 2020). Ruby fluorescence is
226 commonly used as a pressure sensor in DAC experiments, but it was not added to the
227 HDAC experiments as it dissolves quickly in the heated aqueous fluid, possibly causing
228 chemical pollution.

229 (2) In all experiments small gold particles were added into the sample chambers to
230 determine the pressure in-situ with SXR during the run. Gold was measured usually
231 after quenching of the laser heating cycle. The SXR analyses were processed with
232 DIOPTAS (Prescher and Prakapenka, 2015) and the GSAS-II (Toby and Dreele, 2013)
233 software. The pressure shift from the equation of state (EOS) for gold was calculated

234 after Dorogokupets and Dewaele (2007) in the web application
235 <http://kantor.50webs.com/diffraction.htm>. Unlike ruby, the gold flakes do not dissolve in
236 hydrous experiments. In the neon experiments, the addition of gold allowed us to
237 compare it to the ruby fluorescence pressures.

238 (3) For the hydrous experiments LN11 and LN22 the pressure was determined
239 additionally after the run using the EOS for water and following the method described by
240 Bassett et al. (1993). The water-ice phase transition was used to calculate the fluid
241 density in the sample chamber: this was done after the experiment (the HDAC were
242 kept closed) and not during the experimental session at Soleil. The sample chamber of
243 the HDAC was cooled down with liquid nitrogen and the temperature of the phase
244 transition between water and ice VI in the aqueous fluid was measured with the
245 attached thermocouples. Pressures were then calculated from the EOS for the water-ice
246 transition (Wagner and Pruß, 2002). This is feasible as the use of the EOS of water in
247 silicate-water systems has been validated by Munsch et al. (2015). Table 2 lists all
248 calculated pressures from gold, water-ice transition, and ruby.

249 *2.3.2. Challenges in pressure determination*

250 Pressure determination in the HDAC is challenging and was often not satisfying during
251 for the conducted runs. The sample chamber is a closed system during the experiment
252 and once it has been compressed, the pressure inside remains constant if the cell does
253 not leak or the pressure is altered – intentionally or by damaging. While the sample is
254 heated the pressure increases inside the sample chamber due to thermal pressure, but
255 it decreases again after quenching/during cooling of the sample. Therefore, ruby
256 fluorescence in neon experiments shows the same pressure before and after the

257 experiment (at room temperature) and confirms that the system remained close (Table
258 2). To prevent all parts of the loaded cell from damage suffering in hydrous
259 experiments, the nitrogen cooling for pressure determination with the EOS of the water-
260 ice transition was only applied after cessation of the experiment while the HDAC were
261 kept closed. During sample loading of the hydrous experiments no high-pressure
262 polymorphs of ice were observed in any of the loaded sample chambers at room
263 temperature. Thus, none of the HDAC samples exceeded pressures of 1.1 GPa during
264 the pre-experiment compression (c.f. Wagner and Pruß, 2002). The pressure
265 determination from the water EOS is precise and reliable only for the last heating cycles
266 performed in the HDAC. Respectively, the limit $P < 1.1$ GPa is proposed for the first
267 heating cycles of each experiment (Table 1).

268 Most pressures calculated from the EOS for gold do not agree well with the other two
269 methods (Table 2). The pressures measured with gold are in average about 1.2 GPa
270 higher than the pressures determined with water-ice transition or ruby. The difference
271 between gold and both alternative methods show a moderate positive correlation of $r =$
272 0.69 (Figure 2), with -1 or 1 for an excellent correlation and 0 for no correlation.
273 However, the trend in Figure 2 would be expected to match with $m = 1$ (dashed line), as
274 all working pressure calculation methods should give the same results within an error,
275 or it should describe a nonlinear approach to 1 on a larger pressure scale. We used
276 only data points where the pressure was measured under the same conditions with two
277 different methods for Figure 2. The dataset is small, and the range of pressure is limited
278 to < 1.7 GPa (ruby) which lies in the nature of the experiments of this study. A nonlinear
279 approach towards the dashed line ($m = 1$) can be expected for pressures > 2 GPa, but

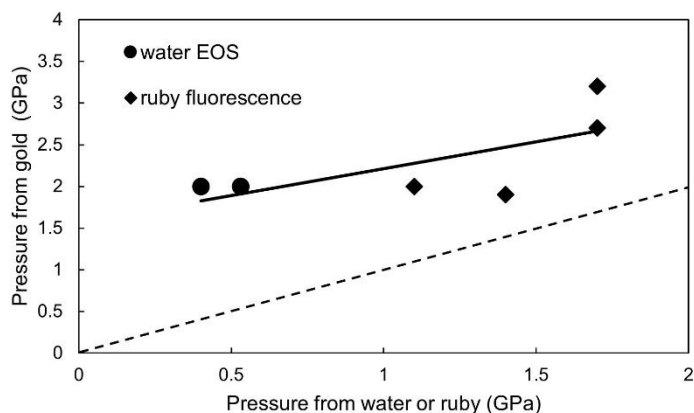
280 at lower pressures the EOS of gold shows a clear shift towards higher pressures (Figure
281 2) and cause probably pressure overestimation.

282 Pressure values calculated from gold show further unexpected behavior during each
283 experiment, as for several runs the pressure seem to remain elevated after the last
284 quenching – relative to the first measured pressure before the start of the experiment.

285 This is not in agreement with ruby fluorescence. Moreover, in experiment LN11 the
286 pressure seems to drop during the laser heating from 1.9 GPa to 0.8 - 1.2 GPa for the
287 first four heating cycles but seem to increase to 2.0 GPa after the last heating cycle
288 (Table 2). A closure (volume change) of the sample chamber could not be observed.

289 We argue therefore that pressure calculations from the EOS of gold are unreliable for
290 the applied pressure range of this study (< 2 GPa). Pressure data in this range
291 calculated from gold XRD are rather estimates and must be handled with care.

292



293

294 Figure 2 Pressures in the DAC sample chamber calculated from the EOS for gold
295 vs. pressures calculated from the EOS for water or from ruby fluorescence. The linear

296 trend (black line) shifts from the expected trend (dashed line) between the applied
297 methods.

298

299 2.4. Starting material composition

300 For the starting material, we used a natural island arc basalt from the Soufriere volcano
301 on St Vincent Island, Lesser Antilles arc (STV301 glass Pichavant et al., 2002) that was
302 enriched in Br and water: The basalt was grounded into a fine grain powder to which 3
303 wt.% of NaBr and 2 wt.% of H₂O were added. We melted the powder in a Boyd &
304 England-type piston cylinder apparatus (Boyd and England, 1960) at the Institut de
305 Physique du Globe de Paris (IPGP) to obtain a glass of this hydrous, Br-bearing basaltic
306 mixture. Synthesis conditions for our starting glass were 1.1 GPa, 1300 °C and 30 min
307 run duration. A sealed Au-Pd capsule prevented major iron loss. Small pieces of the Br-
308 bearing hydrous glass were used for the in-situ experiments. For the aqueous fluid we
309 used distilled water.

310 The synthesized basaltic starting material is texturally homogenous. We used an optical
311 microscope first, and an electron microscope (FEG Zeiss Ultra55) at the IMPMC,
312 Sorbonne Université Paris to check the glass for impurities. The glass looks
313 homogenous and no crystals, gas- or water bubbles could be found. Major and minor
314 elements were analyzed with a JEOL 8530F Plus Electron Probe Microanalyser (EPMA)
315 at the Centre for Advanced Microscopy, ANU in Canberra, Australia and confirmed that
316 the basalt glass is also chemically homogenous. The composition of the starting glass
317 can be found in Table 3. The Br concentration is about 1.1 ± 0.1 wt.% (with EPMA) and

318 was confirmed with Synchrotron X-ray fluorescence (SXRF) in the basalt glass before
319 each experiment.

320

321 2.5. In-situ analysis of Br concentrations

322 Bromine concentration in basalt glass, aqueous fluid, and neon were measured
323 quantitatively by SXRF in situ analysis in the diamond anvil cells (DAC) at the SOLEIL
324 Synchrotron on the PSICHÉ beamline. We used a monochromatic beam of 33 keV that
325 was masked by a pinhole of 50 μm in diameter and focused at 12 x 10 μm^2 . For each
326 experiment the DAC was positioned perpendicular to the beam. Both SXRF and SXRD
327 were detected in transmission geometry. SXRF was detected by a SDD detector which
328 was placed at 24° relative to the beam transmitted through the DAC. Counting times
329 were usually set to 600 seconds.

330 SXRF analyses were calibrated on a 240 μm thick piece of the NIST silicate glass
331 certified reference material SRM 610 (e.g., Rocholl et al., 1997). The Br content in NIST
332 610 is not quantified but NIST 610 is calibrated for multi elemental analyses on glasses
333 and covers a broad range of elements including elements with $K\alpha$ peak energies close
334 to the $K\alpha$ peak of Br (11.9 keV) e.g., Se (11.2 keV), As (10.5 keV) or Sr (14.1 keV). The
335 volcanic glass V1 (Mosbah et al. 1995) was measured additionally as standard glasses,
336 as well as a piece of the Br-H₂O-doped starting glass (BaM024). To test for any effects
337 of DAC setup on SXRF measurements NIST 610 was also placed in the DAC at
338 ambient pressure and temperature. No effects could be found between the different
339 NIST analyses. All glasses show good agreements for their element concentrations in

340 the energy range of Br (Table 4). During the experiments basalt glass analyses were
341 conducted in the center of the heated region (the crater-like texture in neon
342 experiments). The detection limit is typically in the range of of 1-10 $\mu\text{g/g}$, which is in
343 good agreement with similar studies (e.g. Louvel et al., 2020a) and with what can be
344 expected for elements of a similar mass (Rousseau, 2001).

345 The gaskets of each experiment were recovered, and their thickness was measured
346 after the run to calculate the change in the set-up geometry of the SXRF analyses
347 during the experiments. To quantify the Br concentration in the basaltic glass, the
348 aqueous fluid, or in neon all obtained SXRF spectra from standards and experiments
349 were processed by using the PyMCA software (Solé et al., 2007). We compared the Br
350 concentration of the starting material with the calculated values from PyMCA for the first
351 measurement at room temperature for each experiment. If both values were not in
352 agreement, we assumed that the basalt glass was not touching both diamonds. The
353 initial thickness of the glass was then calculated using PyMCA by adding a water/neon
354 layer to fit the calculated Br concentration with the value from the starting material. For
355 matrix corrections we assumed a 2.9 g/cm^3 for basalt, $1\text{-}1.2 \text{ g/cm}^3$ for water and 0.5
356 g/cm^3 for supercritical Neon.

357

358 3. RESULTS

359 3.1. Textural observations

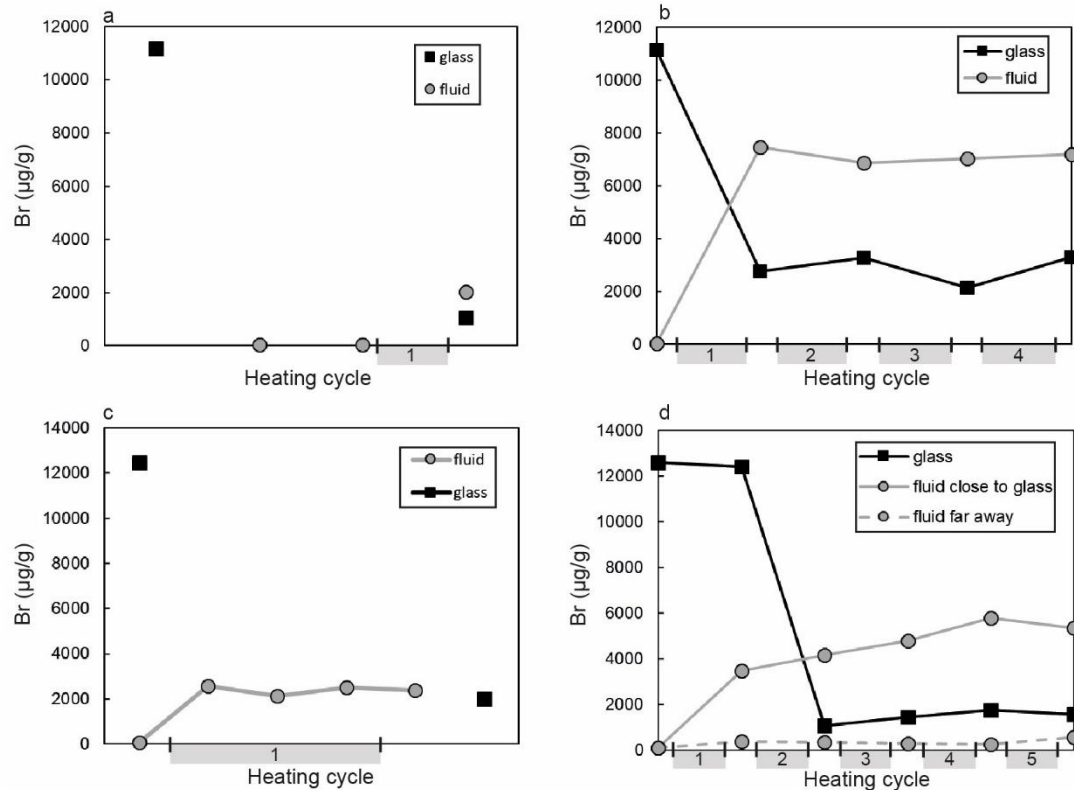
360 Textural changes of the basalt glass were observed after quenching the experiment. In
361 hydrous experiments the glass has a spongy or foam-like texture after the ultra-fast

362 quenching induced by the laser turn off which causes very fast local water exsolution
363 (Figure 1a-b). This transformation into a foam affected a volume that is much larger
364 than the original laser heating spot and is seen at the rim of the glass piece. It shows
365 therefore that almost the whole glassy volume is melted during the heating. These
366 textures have not been observed in studies with haplogranite where the external heating
367 is strong enough to melt the entire glass in the sample chamber of the HDAC and when
368 temperatures decrease slowly (Bureau et al., 2010; Louvel et al., 2020b). The spongy
369 textures were not found in neon runs. As a study from Balcone-Boissard et al. (2020)
370 shows, bromine diffusion in related melts is much lower than that of H₂O. External
371 heating was added to lower the temperature gradient and to support the
372 homogenization of the hydrothermal fluid in several experiments, but temperatures were
373 not high enough to melt the entire piece of glass or even reach full miscibility between
374 melt and fluid. Nevertheless, experiments like LN11 and LN22 for water show
375 reproducible results and equilibration between the Br concentration in the glass and in
376 the surrounding fluid within their runs.

377 In neon experiments the melting spots of the laser are clearly visible but the glass
378 around the laser appears to be texturally unharmed (Figure 1c-d). The temperature
379 gradient is larger than in the hydrous experiments because no external heating was
380 applied to the CDAC. However, the basalt glass shows no strong reaction with neon.

381 All experimental results are listed in Table 1.

382



383

384 Figure 3 Bromine concentration versus time/heating cycles in hydrous experiments.

385 During each heating cycle step the basalt glass was melted, quenched, and analyzed

386 again. a) Cpo2: Already the first heating cycle reduces the Br concentration in the basalt

387 dramatically. b) LN22: Bromine concentrations in the basalt glass and in the aqueous

388 fluid equilibrate quickly after quenching the first heating cycle and remain on relatively

389 constant levels. The plateau of the curve is a good indicator for chemical equilibrium. c)

390 Cpo3: Bromine concentration in the aqueous fluid equilibrates quickly and remains

391 constant after quenching. d) LN11: Without the usage of external heating the

392 concentration of bromine in the aqueous fluid is not homogenized and shows a distinct

393 difference between the concentrations analyzed close to the melted glass and further

394 away.

395

396 3.2. Hydrous Experiments

397 3.2.1. Run Cpo2

398 Run Cpo2 shows Br loss to the surrounding aqueous fluid: Br concentration before the
399 first heating is 11160 $\mu\text{g/g}$ in the glass and 26-48 $\mu\text{g/g}$ in the fluid. For this run the
400 temperature of the laser could not be measured precisely. After quenching the
401 concentration changes to 1070 $\mu\text{g/g}$ in the glass and 2029 $\mu\text{g/g}$ in the fluid (Figure 3a).
402 A partition coefficient of $D_{\text{fluid/glass}}^{\text{Br}} = 1.9$ was calculated. The pressure could not be
403 determined precisely, but according to the stability of water and ice VI at room
404 temperature the pressure in the loaded cell is < 1.1 GPa (Wagner and Pruß, 2002).
405 Gold SXRD gave a pressure range of 2.6 GPa before the heating and 2.1 GPa after the
406 heating.

407 3.2.2. Run LN22

408 In run LN22 Br concentration before the first heating is 11120 $\mu\text{g/g}$ in the glass and 18
409 $\mu\text{g/g}$ in the aqueous fluid. The laser temperature could only be estimated but SXRD
410 confirmed that it was above the solidus of the hydrous basalt. After quenching the
411 concentrations change to 2124-3282 $\mu\text{g/g}$ in the glass and 6864-7455 $\mu\text{g/g}$ in the fluid
412 for all four cycles (Figure 3b). A range of $D_{\text{fluid/glass}}^{\text{Br}} = 2.10 - 3.31$ was calculated. The
413 pressure range is between 0.4 and 1.1 GPa during the experiment according to water
414 and decreased slightly from 2.1 GPa to 2.0 GPa according to gold.

415 Br concentration in water and basalt reach a plateau after the first heating cycle (Figure
416 3b). This is a good indicator that chemical equilibrium has been reached in the
417 experiment.

418 3.2.3. *Run Cpo3*

419 In run Cpo3 Br concentration is 12440 $\mu\text{g/g}$ in the glass and 79 $\mu\text{g/g}$ in the aqueous fluid
420 before the heating. While the laser keeps the basalt liquid, the Br concentration in the
421 fluid ranges from 2130 to 2563 $\mu\text{g/g}$. After quenching the concentrations is 1990 $\mu\text{g/g}$ in
422 the glass and 2370 $\mu\text{g/g}$ in the fluid (Figure 3c). A value of $D^{\text{Br}}_{\text{fluid/glass}} = 1.19$ can be
423 calculated. According to run Cpo3 there are no notable changes in Br concentration
424 before and after quenching the glass. As for run Cpo2 the pressure is < 1.1 GPa
425 according to water but increases from 1.6 GPa to 2.1 GPa according to gold.

426 3.2.4. *Run LN11*

427 Bromine concentration before the first heating is 12610 $\mu\text{g/g}$ in the glass and 80 $\mu\text{g/g}$ in
428 the aqueous fluid. After the first quenching the Br concentration remains high in the
429 glass (12410 $\mu\text{g/g}$) but becomes slightly lower after heating-quenching cycle 2-5 (1062-
430 1752 $\mu\text{g/g}$). In the fluid, measurements close to the melted glass show that the Br
431 concentration ranges from the first to the fifth quenching between 3462 and 5784 $\mu\text{g/g}$.
432 Further away from the glass, the values range from 226 to 565 $\mu\text{g/g}$ (Figure 3d). While
433 Br shows a concentration gradient the partitioning between fluid and glass remains
434 relatively constant in cycle 2-5 with $D^{\text{Br}}_{\text{fluid/glass}} = 3.30$ to 3.92 close to the glass and
435 $D^{\text{Br}}_{\text{fluid/glass}} = 0.13$ to 0.37 at the rim of the sample chamber. The pressure range is
436 between 0.53 and 1.1 GPa calculated from water EOS and varies between 0.8 and 2.0
437 GPa calculated from the EOS for gold.

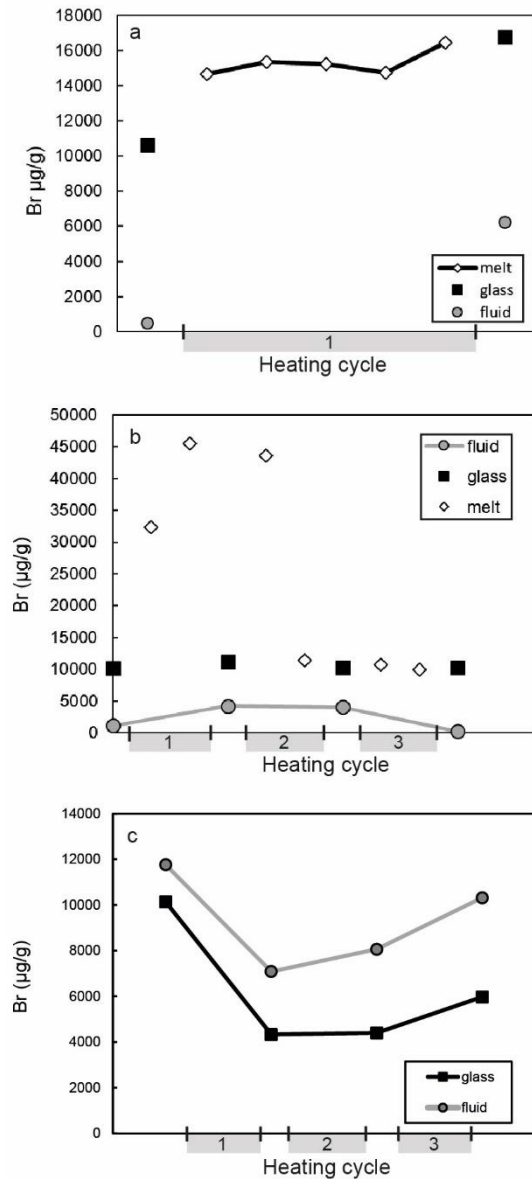
438

439 3.3. Neon Experiments

440 3.3.1. *Run Mar1*

441 In run Mar1 bromine concentration before the first heating is 10620 µg/g in the glass
442 and 209 µg/g in the neon. During laser heating the concentration increases slightly from
443 14640 to 16430 µg/g in the melt. It remains high (16430 µg/g) in the quenched glass
444 and increased in the neon to 16212 µg/g (Figure 4a). A partition coefficient of $D_{\text{neon/glass}}^{\text{Br}}$
445 = 0.37 can be calculated from the Br values in the fluid and in the glass. The pressure is
446 1.7 GPa according to ruby fluorescence and increases from 2.7 to 3.2 GPa according to
447 the EOS of gold. We assume that the observed change in concentration comes from
448 slight variation in the glass thickness between the different heating cycles. The melt can
449 become spherical and might have extended further in the direction of the beam within
450 the sample chamber. While Br concentration increased during the ongoing melting the
451 calculated partitioning between glass and fluid is in good agreement with the Hak1 run
452 (see below).

453



454

455 Figure 4 Bromine concentration versus time/heating cycles in neon experiments.
 456 During each further heating cycle step the basalt glass was melted, quenched, and
 457 analyzed again. a) Mar1: Br concentrations remain high in the basalt glass and low in
 458 the neon. No changes in concentration appear between melt and glass. b) Hak1: The
 459 bromine concentrations measured in the neon remain lower than in the basalt glass.
 460 With ongoing decompression water is released from the hydrous basalt glass during the
 461 last heating cycle. We suspect bromine to partition into the released water while neon

462 remains depleted in bromine. c) Hak2: Bromine concentration remain higher in the neon
463 than in the basalt glass over all heating cycles.

464

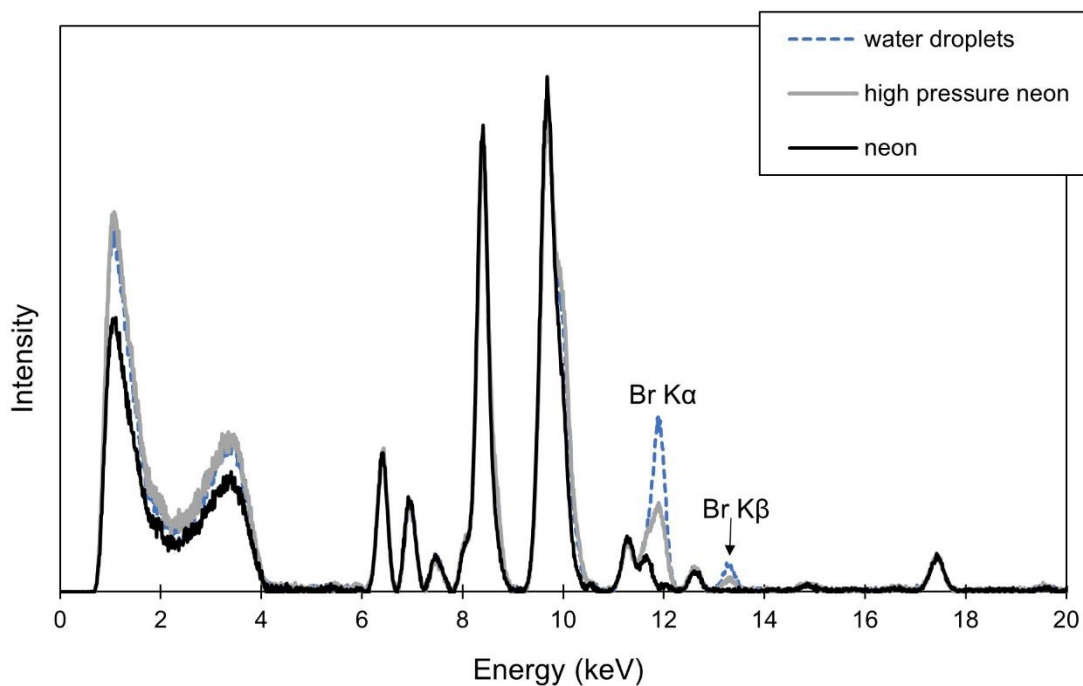
465 3.3.2. Run Hak1

466 In run Hak1 bromine concentration before the first heating is 10019 $\mu\text{g/g}$ in the glass
467 and 1062 $\mu\text{g/g}$ in the neon. During the first heating cycle Br concentration ranges from
468 11019 $\mu\text{g/g}$ to 45065 $\mu\text{g/g}$ in the melt and in the quenched glass respectively. In the
469 second and third heating cycles Br concentration remains lower in the melt and in the
470 glass ranging from 9864 $\mu\text{g/g}$ to 11256 $\mu\text{g/g}$. In the neon the measured Br concentration
471 increases to 4153 $\mu\text{g/g}$, 3985 $\mu\text{g/g}$, and 208 $\mu\text{g/g}$ after each of the three quenching
472 cycles. Currently, we cannot fully explain the high Br values in the melt for the first two
473 heating cycles. Volume changes during the melting could explain the variations.
474 However, in heating cycle 2 and 3 the Br values decrease and equilibrate with the
475 values measured in the glass. The $D^{\text{Br}}_{\text{neon/glass}}$ values are 0.38, 0.39, and 0.02,
476 respectively (Figure 4b).

477 The pressure is 1.1 GPa after loading the cell measured with ruby fluorescence or 3.3
478 GPa with gold. At this pressure the diffraction peaks also overlap with neon at 1.2 GPa.
479 Like in all other experiments with neon, the external pressure (1.1 GPa) is released
480 stepwise between each heating-quenching cycle. After the last quenching small droplets
481 of water could be observed as a third phase in the sample chamber (Figure 1d; Figure
482 5). This observation suggests a pressure < 1.1 GPa after the last quenching but will be

483 discussed in more detail further below. The calculated pressure from gold is 3.1 GPa
484 (1.2 GPa from neon) at the end of the experiment.

485



486

487 Figure 5 Synchrotron X-ray fluorescence analysis of the pressure medium in run
488 Hak1. High pressure neon was analyzed at heating cycle 2 while water was absent. The
489 Br concentration in the HP neon is 4025 $\mu\text{g/g}$ (grey). When the pressure was decreased
490 in heating cycle 3 water bubbles released from the hydrous basalt could be observed in
491 the neon (c.f. Figure 1d). With the presence of water Br concentrated in the water
492 bubbles (blue) and decreased in the neon down to 210 $\mu\text{g/g}$ (black).

493

494 3.3.3. Run Hak2

495 For run Hak2 the closed cell with the sample Hak1 was recompressed and used again
496 for three heating-quenching cycles. Bromine concentration before the first heating is
497 10138 $\mu\text{g/g}$ in the glass and already high in the neon from the former run Hak1 with
498 11760 $\mu\text{g/g}$. After quenching the concentrations range from 4333 to 5974 $\mu\text{g/g}$ in the
499 glass and 7087 to 10314 $\mu\text{g/g}$ in the fluid (Figure 4c). A range of $D^{\text{Br}}_{\text{fluid/glass}} = 1.64 -$
500 1.83 can be calculated. The ratio calculated from the Br concentrations before the first
501 heating in this experimental run is $D^{\text{Br}}_{\text{fluid/glass}} = 1.16$. The pressure determined with ruby
502 spheres is 1.4 GPa before the first and after the last run. Gold pressure determination
503 decreased from 2.8 GPa to 1.9 GPa.

504

505 4. DISCUSSION

506 4.1 Bromine partitioning between basalt and aqueous fluids

507 The fluid-melt partitioning values from our experiments range from $D^{\text{Br}}_{\text{fluid/melt}} = 1.19$ to
508 3.31 ± 0.6 – within the applied pressure and temperature range. These values overlap
509 with findings from other studies but are slightly lower than the partition coefficients
510 calculated by Bureau et al. (2010), Cadoux et al. (2018), and Louvel et al. (2020b).
511 Partition coefficients between haplogranite and an aqueous fluid from Bureau et al.
512 (2010) range from $D^{\text{Br}}_{\text{fluid/melt}} = 2.18 \pm 0.4$ to 15.3 ± 2 and values from Louvel et al.
513 (2020b) range from $D^{\text{Br}}_{\text{fluid/melt}} = 2 \pm 0.2$ to 9.2 ± 1.8 . Cadoux et al (2018) found partition
514 coefficients of $D^{\text{Br}}_{\text{fluid/melt}} = 3.8$ to 5.2 from their experiments with basaltic composition
515 and 8.6 to 27.9 from rhyodacite. With all calculated $D^{\text{Br}}_{\text{fluid/melt}} > 1$ the data from all four

516 studies confirm that Br has a slight to strong affinity to partition from the melt into the
517 aqueous fluid.

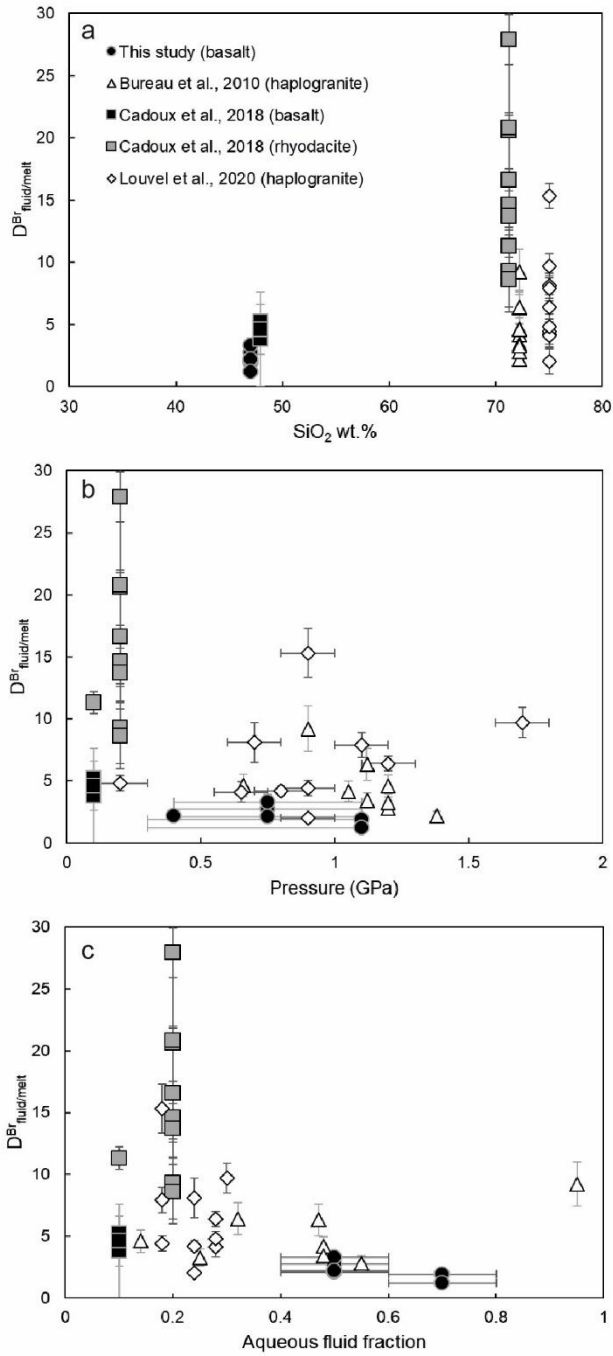
518 Partition coefficients from Cadoux et al. (2018) are generally higher than partition
519 coefficients from the other three studies for comparable SiO₂ content (Figure 6). One
520 reason could be that Cadoux et al (2018) did not conduct in-situ experiments and
521 measured Br concentrations only in the quenched samples. In fact, the three other
522 studies are all conducted and analyzed in-situ in HDAC – this study at least partially.
523 Louvel et al. (2020b) argue that differences in the partition coefficients to Cadoux et al.
524 (2018) might come from the quantification of Br by mass balance as it was used by
525 Cadoux et al. (2018), or artifacts of the quench cooling that cause Br loss into the fluid.
526 Louvel et al. (2020b) exclude their data point at 0.2 GPa, as they suspect uncertainties
527 in the pressure determination below 0.5 GPa. Run Hak1 demonstrates that Br
528 concentrations do not change significantly in our experiments in neon between basalt
529 melt and quenched basalt glass (Figure 4b), but it can be the case with water in
530 externally heated DAC experiments up to 800-900 °C (e.g., Borchert et al., 2009;
531 Bureau et al., 2010; Leroy et al., 2019). At these temperatures external heating
532 increases the pressure in the sample chamber. Quenching the experiment can induce a
533 pressure drop that affects the partitioning of elements like Sr, Rb, (Borchert et al., 2009)
534 or Br (e.g., Bureau et al., 2010). Due to the selective heating of the laser, the pressure
535 increase in the cell is small and fast diffusion during cooling plays a minor role in our
536 experiments. Therefore, differences might also come from uncertainties in pressure
537 determination or Br quantification in quenched samples.

538 Several trends for partition coefficients were described and suggested in existing
539 studies on Br partitioning (e.g., Figure 6): Bureau et al (2010) found correlations of
540 decreasing $D_{\text{fluid/melt}}^{\text{Br}}$ with increasing pressure and with increasing water content.
541 Cadoux et al (2018) found a correlation of decreasing $D_{\text{fluid/melt}}^{\text{Br}}$ with increasing
542 temperature and with decreasing SiO_2 concentration within their data. This
543 compositional effect of the melt was also described by Bureau and Metrich (2003) and
544 Cochain et al. (2015). Louvel et al., 2020b found the variation in the partition coefficients
545 to remain small over a large P-T range and do not find any clear trend. They propose
546 that hydrous granite melts have a Br storage capacity similar to aqueous fluids. This
547 makes sense as with increasing pressure and temperature, both fluid and melt tend to
548 be equal before being miscible (Bureau and Keppler, 1999). This could buffer changing
549 P-T conditions to some extent. Assuming a compositional trend, the basalt from Cadoux
550 et al. (2018) has a higher $D_{\text{fluid/melt}}^{\text{Br}}$ than values from this study, which rather overlaps
551 with the partition coefficients from the haplogranite of Bureau et al. (2010). The
552 rhyodacite from Cadoux et al. (2018) has about the same amount of SiO_2 as the
553 haplogranite but has higher $D_{\text{fluid/melt}}^{\text{Br}}$ values. This can be best explained with the
554 pressure trend described by Bureau et al. (2010).

555 As the partition coefficients for basalts are generally smaller than for SiO_2 -rich melts, the
556 data from Cadoux et al. (2018) and from this study support the pressure trend, as well
557 as the general trend of decreasing $D_{\text{fluid/melt}}^{\text{Br}}$ with increasing water content. However,
558 given the uncertainties and the data spreading from all five studies and the much
559 stronger effect melt composition, it is not clear if pressure, melt composition, or fluid
560 fraction have the strongest effect on the partitioning.

561

562



563

564 Figure 6 Aqueous fluid-melt partition coefficients for bromine from Bureau et al.

565 (2010) (triangle), Cadoux et al. (2018) (box), Louvel et al. (2020b) (diamond) and this

566 study (Cpo2, Cpo3, LN22 in circles) vs. a) SiO₂ content in the silicate glass; b) vs.
567 pressure; c) vs. aqueous fluid fraction.

568

569 4.2. Bromine partitioning between basalt glass and neon

570 The calculated neon-melt partition coefficients in the experiments Hak1 and Mar1 are in
571 the range of $D_{\text{fluid/melt}}^{\text{Br}} = 0.38 \pm 0.06$ and imply that Br favors to remain in the basalt
572 liquid over partitioning into the neon, an inert fluid phase (Table 1). To the authors'
573 knowledge there are no further studies on halogen partitioning between a silicate glass
574 and neon or any other dry gaseous phase such as CO₂. We argue that Br has a strong
575 affinity to bond with water but a low affinity to bond with neon which can be a good
576 analogue for CO₂, the second major volatile degassed by volcanoes. Both neon and
577 CO₂ do not have a strong bonding affinity to halogens. Therefore, Br tends to remain in
578 the basaltic melt. However, partition coefficients from experiment Hak2 range from 1.16
579 to 1.83. This discrepancy within the neon-related experiments needs to be addressed:

580 We used a hydrous basalt with about 2 wt.% of H₂O as starting material for the
581 experiments of this study. In experiment Hak1 water droplets released from the hydrous
582 basalt could be observed in the sample chamber after the last heating cycle (Figure 1d;
583 Figure 5). The water droplets were visible at the end of run Hak1 and could explain the
584 decrease of Br concentration in the neon from 3985 to 208 µg/g Br after the last heating
585 cycle: As soon as small amounts of water appear as a third phase in the sample
586 chamber, Br partitions from neon into water leaving the neon fluid with much lower Br
587 concentration than in the former heating-quenching cycles.

588 The cell remained closed for the next experiment Hak2 but after recompression of the
589 cell the water droplets could not be observed during the experiment Hak2. At ≥ 1.4 GPa
590 and ambient temperature liquid water is not stable but instead ice VI (Wagner and Pruß,
591 2002). However, neither water nor ice VI were observed before and during the Hak2
592 experiment. In the lack of Br partitioning data between ice VI and neon we assume that
593 not much Br can be incorporated in the structure of ice VI and that most of the Br goes
594 back into neon when water transforms into ice during the re-compression of the sample.

595 The partition coefficients between basalt and (dry) neon are represented by the first two
596 heating cycles of Hak1 (0.38 and 0.39) before water droplets were observed. The higher
597 partition coefficients over several heating-quenching cycles in Hak2 (1.16 – 1.83) must
598 be related to the presence of water. At this stage the basalt crossed the glass transition
599 several times (heating and quenching cycles) and Br should partition from the neon
600 back into the basalt while the system equilibrates. Instead, Br concentrations and
601 $D_{\text{neon/glass}}^{\text{Br}}$ remain higher than in Hak1.

602 A mixed fluid of “wetted” or hydrous neon probably explains the elevated concentrations
603 and partitioning values. During heating of the Hak2 experiment neon takes up the water
604 (initially stored in liquid droplets or ice) and increases its Br storage capacity as it
605 becomes slightly hydrous. In Hak1 the water release from the basalt liquid has been
606 initially prevented by the high pressure in the first cycles. After external decompression
607 in the last cycle of Hak1 water could be released from the basalt glass. This is a very
608 likely scenario as the water solubility in the basalt glass strongly relies on pressure (e.g.,
609 Dixon et al., 1995). As the basalt dehydrates during the melting, experiments with dry
610 basalt would be needed to clarify Br behavior in neon.

611

612 4.3 Volcanic bromine degassing and global bromine fluxes

613 Bromine concentrations in natural melts, fluids, or volcanic gases are usually in the
614 range of low $\mu\text{g/g}$. Monitoring of Br cycling, or volcanic degassing remains challenging,
615 and so far, the data are scarce relative to e.g., the lighter halogens fluorine (F) and Cl
616 (e.g., Webster et al., 2018). To calculate a (global) flux for volcanic halogen degassing,
617 two methods can be applied: (1) Volatile degassing can be measured directly at active
618 volcanoes or (2) halogen concentration in melt inclusions can be studied as a
619 petrological approach (for detailed reviews of both methods: Wallace, 2005; Pyle and
620 Mather, 2009; Webster et al., 2018, and references therein).

621 4.3.1. Volcanic halogen degassing

622 Halogen flux calculations from present-day emissions have been applied to accessible
623 volcanoes – most of them are related to arc volcanism (Pyle and Mather, 2009). Due to
624 its high concentration in volcanic gasses SO_2 is the easiest volatile to measure in
625 volcanic plumes. Measured halogen concentrations can be scaled up using e.g.,
626 HF/SO_2 or HCl/SO_2 ratios (Wallace, 2005). For Br either HBr/HCl or HCl/SO_2 are
627 commonly in use as ratios. However, halogen- and SO_2 degassing show large spatial
628 variations and can vary dramatically at one volcano during different phases of activity
629 (c.f. Edmonds et al., 2001, 2002). This can have large impacts on global flux upscaling
630 (Pyle and Mather, 2009, Webster et al., 2018, Cadoux et al., 2022). Recent flux
631 estimates for halogens from volcanic gas data range therefore over two orders of

632 magnitude for F and Cl, and over four orders of magnitude for Br and iodine (Webster et
633 al., 2018).

634 Several values for global Br flux from volcanic arc degassing have been calculated
635 based on HBr measurements and the comparison to HBr/HCl or HCl/SO₂ ratios: Halmer
636 et al. (2002) calculated $2.6-43.2 \times 10^9$ g/y, Aiuppa et al. (2005) calculated 13×10^9 g/y,
637 Pyle and Mather (2009) calculated $5-15 \times 10^9$ g/y, and Webster et al. (2018) calculated
638 10.5×10^9 g/y (Table 5). Several studies on volatile degassing show that halogen
639 degassing from non-arc volcanism is rather negligible for global flux calculations of e.g.,
640 Cl (5.5 wt. % of the annual global flux) and for heavy halogens like Br (0.6 wt. %;
641 Webster et al., 2018; with data from: Gerlach, 2004; Aiuppa et al., 2009; Shinohara,
642 2013).

643 *4.3.2. Global flux calculation from melt inclusions*

644 The calculation of global halogen flux from melt inclusions compares the concentration
645 of halogens measured in pre-eruptive melt inclusions with post-eruptive glass of the
646 final degassed lava (e.g., Webster et al., 2018; d'Augustin et al., 2020). This approach
647 allows to estimate volatile flux from volcanic eruption of the past. Chlorine and fluorine
648 exsolve at low pressures with < 100 MPa for Cl and < 10 MPa for F (Aiuppa et al., 2009;
649 Webster et al., 2018). This implies late degassing of both halogens during magma
650 ascent and a good preservation of initial Cl and F contents in pre-eruptive melt
651 inclusions. Not much is known about the behavior of Br but the small pressure effect on
652 melt-fluid partitioning in basalts suggests also shallow degassing of Br.

653 Following the method described in Wallace (2005), we can calculate an annual bromine
654 flux q_{Br} :

$$q_{\text{Br}} = \frac{Q \times \rho_B}{c_{\text{fl}}}$$

655 with ρ_B as the density for basalt (2.8 g/cm³). For the annual magma flux Q , we use a
656 global arc magma flux of 2.5×10^{15} cm³/y from Carmichael (2002). Instead of using Br
657 measurements from post-erupted glasses, the bromine concentration in the
658 fluid/degassing phase c_{fl} can be calculated as

$$c_{\text{fl}} = c_{\text{mi}} \times W \frac{D}{D + 1}$$

659 with c_{mi} as bromine concentration in melt inclusions and D as the newly gained partition
660 coefficient $D^{\text{Br}}_{\text{fluid/melt}}$ for aqueous fluid experiments from this study. The addition of the
661 factor W considers that the fluid fraction in our experiments is higher than in natural
662 systems: Experiments from this study have a fluid fraction of 25 to 45 wt.%. Arc
663 magmas can have water contents up to 20 wt.%, but probably not all over the globus
664 (Urann et al., 2022). Assuming a water content between 5 and 12 wt.% would lead to a
665 factor $W = 3$ to 7.

666 The amount of data for bromine concentration in melt inclusions (c_{mi}) are rather limited
667 relative to the lighter halogens F and Cl. Webster et al. (2018) compiled a dataset of
668 175 measurements for Br and 4710 measurements for Cl in melt inclusions. They find
669 that primitive arc magmas have in general Br concentrations < 10 µg/g. Higher
670 concentrations are however possible: Straub and Layne (2003) found melt inclusions
671 with Cl concentration of 9400 µg/g from the Izu Bonin arc. According to typical Cl/Br

672 mantle ratios of about 300, primitive melts at the Izu Bonin arc could have Br
673 concentrations of 30 $\mu\text{g/g}$ (Bureau et al., 2010). But for a global Br distribution in
674 primitive arc magmas an average concentration of 5 $\mu\text{g/g}$ is more likely (e.g., dataset
675 from Webster et al., 2018) and is also in good agreement with other recent findings with
676 about 3-5 $\mu\text{g/g}$ Br in melt inclusions from arc basalts (Kutterolf et al., 2013; Vidal et al.,
677 2016).

678 With 5 $\mu\text{g/g}$ as initial average Br concentration the calculated global Br flux from arc
679 volcanoes ranges from 23.5×10^9 g/y to 72.9×10^9 g/y in respect to the minimum and
680 maximum values of our experimentally determined partition coefficients $D_{\text{fluid/glass}}^{\text{Br}} =$
681 1.19 and $D_{\text{fluid/glass}}^{\text{Br}} = 3.92$ and the water content of arc magmas. The calculated flux is
682 higher than values from degassing data (Table 5), but these values could be
683 underestimated as they assume a SO_2 fluxes of 14×10^{12} g/y (Aiuppa et al., 2005),
684 15×10^{12} g/y (Pyle and Mather, 2009), 16.8×10^{12} g/y (Webster et al., 2018), or 16.8×10^{12}
685 g/y (Cadoux et al., 2022) for their calculations of the Br flux. Recent findings of a higher
686 SO_2 flux of $23 \pm 2 \times 10^{12}$ g/y (Carn et al., 2017) would lead also to higher results for
687 corrected Br degassing values with fluxes of 21.4×10^9 g/y, $8\text{-}23 \times 10^9$ g/y, 14.4×10^9 g/y,
688 or 12.3×10^9 g/y, respectively (Table 5). Given all uncertainties for volatile flux
689 estimations in general, these values for the global Br flux and the newly calculated flux
690 based on our experiments are in a very good agreement.

691

692 5. CONCLUSION

693 We present a new experimental dataset for Br partitioning between basalt and an
694 aqueous fluid and between basalt and neon. To our knowledge these are the first
695 experimental data measured in-situ for Br degassing from basalt. We calculated
696 partition coefficients of $D^{\text{Br}}_{\text{fluid/melt}} = 1.19$ to 3.92 at 0.4 to 1 GPa for magma degassing in
697 water-rich magmas (aqueous fluids in equilibrated experiments). The values are in good
698 agreement with partition coefficients from ex-situ experiments at lower pressures with
699 basalt (Cadoux et al., 2018) and confirm a slight negative correlation with pressure, as
700 well as a strong positive correlation with SiO_2 content.

701 Experiments with an inert gas analogue for CO_2 as pressure medium (neon) give
702 partition coefficients < 1 ($D^{\text{Br}}_{\text{fluid/melt}} = 0.38 \pm 0.01$ at 1.1 GPa) for magma degassing
703 under almost dry (2 wt.% water) conditions, as neon and Br have no bonding affinity.
704 These experiments propose less Br degassing for e.g., dry intra-plate volcanism relative
705 to hydrous eruptions in arcs, in good agreement with natural observations.

706 From the calculated partition coefficients for the presented anhydrous experiments and
707 from global Br concentration values in melt inclusions from arc magmas, we calculated
708 a global Br flux of $23.5 - 72.9 \cdot 10^9$ g/y. This flux is higher than most values calculated
709 from active volcano degassing (Aiuppa et al., 2005; Pyle and Mather, 2009; Webster et
710 al., 2018) but agrees well with new findings on global SO_2 degassing (Carn et al., 2017).
711 Former calculated fluxes may be slightly underestimating the annual Br degassing.

712

713 6. ACKNOWLEDGEMENTS

714 This project was funded by the ANR Projet de Recherche Collaborative VOLC-HAL-
715 CLIM (Volcanic Halogens: from Deep Earth to Atmospheric Impacts), ANR-18-CE01-
716 0018 (Hélène Bureau). Tobias Grützner is grateful for an EU Marie Skłodowska-Curie
717 Fellowship “ExCliso” (Project ID 101017762). We thank the PSICHÉ staff at SOLEIL for
718 their assistance. Paraskevas Parisiadis is thanked for his help with the laser heating test
719 runs we performed at the IMPMC. We thank Marion Louvel, Richard W Thomas, and
720 the two reviewers for their helpful comments to improve the manuscript. Editor Claudia
721 Romano is thanked for handling the manuscript. The authors acknowledge the facilities,
722 and the scientific and technical assistance of Microscopy Australia at the Centre of
723 Advanced Microscopy, The Australian National University.

724

725 7. Appendix A. Supplementary Material

726 The supplementary material contains the raw data of all SXRF spectra and SXRD
727 pattern that were analyzed and processed in this study.

728

729 8. REFERENCES

- 730 Aiuppa, A., Baker, D.R., Webster, J.D. 2009. Halogens in volcanic systems. *Chem.*
731 *Geol.* **263**,1–8.
- 732 Aiuppa, A., Federico, C., Franco, A., Giudice, G., Gurrieri, S., Inguaggiato, S., Liuzzo,
733 M., McGonigle, A.J. S. & Valenza, M., 2005. Emission of bromine and iodine from
734 Mount Etna volcano. *Geochem. Geophys. Geosyst.* **6**, Q08008.
- 735 Balcone-Boissard, H., Baker, D.R., Villemant, B., Caudiz, J., Boudon, G., Deloule, E.,
736 2020. Br diffusion in phonolitic melts: Comparison with fluorine and chlorine diffusion.
737 *Am. Mineral.* 105(11), 1639-1646.
- 738 Bassett, W.A., 2003. High pressure-temperature aqueous systems in the hydrothermal
739 diamond anvil cell (HDAC). *Eur. J. Mineral.* **15**, 773–780.
- 740 Bassett, W.A., Shen, A.H., Buckum, M., 1993. A new diamond anvil cell for
741 hydrothermal studies to 2.5 GPa and from -190°C to 1200°C, *Rev. Sci. Instrum.* **64**
742 2340-2345.
- 743 Bobrowski, N., Hönninger, G., Galle, B., Platt, U., 2003. Detection of bromine monoxide
744 in a volcanic plume. *Nature*, **423**, 273-276.
- 745 Bobrowski, N., Giuffrida, G., 2012. Bromine monoxide/sulphur dioxide ratios in relation
746 to volcanological observations at Mt. Etna 2006-2009. *Solid Earth* **3**, 433-445.
- 747 Borchert, M., Wilke, M., Schmidt, C., Rickers, K., 2009. Partitioning and equilibration of
748 RB and Sr between silicate melts and aqueous fluids. *Chem. Geol.* **259**, 39.

749 Boyd, F.R. and England, J.L., 1960. Apparatus for phase-equilibrium measurements at
750 pressures up to 50 kilobars and temperatures up to 1750 °C. *J. Geophys. Res.* **65**,
751 741–748.

752 Bureau, H., Keppler, H., 1999. Complete miscibility between silicate melts and hydrous
753 fluids in the upper mantle: experimental evidence and geochemical implications. *Earth*
754 *Planet. Sci. Lett.* **165 (2)**, 187-196.

755 Bureau, H, Métrich, N., 2003. An experimental study of bromine behaviour in water-
756 saturated silicic melts. *Geochim. Cosmochim. Acta* **67**, 1689-1697.

757 Bureau, H., Foy, E., Raepsaet, C., Somogyi, A., Munsch, P., Simon, G., Kubsky, S.,
758 2010. Bromine cycle in subduction zones through in situ Br monitoring in diamond
759 anvil cells. *Geochim. Cosmochim. Acta* **74**, 3839–3850.

760 Bureau, H., Auzende, A.-L., Marocchi, M., Raepsaet, C., Munsch, P., Testemale, D.,
761 Mézouar, M., Kubsky, S., Carrière, M., Ricolleau, A., Fiquet, G., 2016. Modern and
762 past volcanic degassing of Iodine. *Geochim. Cosmochim. Acta* **173**, 114–125.

763 Carmichael, I.S.E., 2002. The andesite aqueduct: perspectives on the evolution of
764 intermediate magmatism in west-central (105-998W) Mexico. *Contrib. Mineral. Petrol.*
765 **143**, 641 – 663.

766 Cadoux, A., Tegtmeier, S., Aiuppa, A., 2022. Natural halogen emission to the
767 atmosphere: sources, flux, and environmental impact. *Elements* **18(1)**, 27-33.

768 Cadoux, A., Iacono-Marziano, G., Scaillet, B., Aiuppa, A., Mather, T.A., Pyle, D.M.,
769 Deloule, E., Gennaro, E., Paonita, A., 2018. The role of melt composition on aqueous

770 fluid vs. silicate melt partitioning of bromine in magmas. *Earth Planet. Sci. Lett.* **498**,
771 450-463.

772 Chervin, J.C, Canny B., Besson, J. M., Pruzan, P., 1995. A diamond anvil cell for IR
773 microspectroscopy. *Rev. Sci. Instrum.* **66** (3), 2595-2598.

774 Chervin J.C., Canny B., Mancinelli M., 2001. Ruby-spheres as pressure gauge for
775 optically transparent high pressure cells. *High Press. Res.*, **21**, 305–314.

776 Cochain, B., Sanloup, C., de Grouchy, C., Crépisson, C., Bureau, H., Leroy, C., Kantor,
777 I., Irifune, T., 2015. Bromine speciation in hydrous silicate melts at high pressure.
778 *Chem. Geol.* **404**, 18-26.

779 Couzinet, B., Dahan, N., Hamel, G., Chervin, J.C., 2003. Optically monitored high-
780 pressure gas loading apparatus for diamond anvil cells. *High Press. Res.* **23**, 409-415.

781 d'Augustin, T., Balcone-Boissard, H., Boudon, G., Martel, C., Deloule, E., Bürckel, P.,
782 2020. Evidence for an Active, Transcrustal Magma System in the Last 60 ka and
783 Eruptive Degassing Budget (H₂O, CO₂, S, F, Cl, Br): The Case of Dominica.
784 *Geochem. Geophys. Geosys.* **21**, e2020GC009050.

785 Dixon, J.E., Stolper, E.M., Holloway, J.R., 1995. An Experimental Study of Water and
786 Carbon Dioxide Solubilities in Mid-Ocean Ridge Basaltic Liquids. Part I: Calibration
787 and Solubility Models. *J. Petrol.* **36**, 1607-1631.

788 Dorogokpets, P.I., Dewaele, A., 2007. Equations of state of MgO, Au, Pt, NaCl-B1, and
789 NaCl-B2: Internally consistent high-temperature pressure scales. *High Press. Res.* **27**,
790 431-446.

791 Edmonds, M., Pyle, D., Oppenheimer, C., 2001. A model of degassing at the Soufrière
792 Hills Volcano, Montserrat, West Indies, based on geochemical data. *Earth Planet. Sci.*
793 *Lett.* **186**, 159–173.

794 Edmonds, M., Pyle, D.M., Oppenheimer, C., 2002. HCl emissions at Soufrière Hills
795 Volcano, Montserrat, West Indies, during a second phase of dome building: November
796 1999 to October 2000. *Bull. Volcanol.* **64**, 21–30.

797 Fehn, U., 2012. Tracing crustal fluids: Applications of natural ^{129}I and ^{36}C . *Annu. Rev.*
798 *Earth Planet. Sci.* **40**, 45–67.

799 Gerlach, T.M., 2004. Volcanic source of tropospheric ozone-depleting trace gases.
800 *Geochem. Geophys. Geosyst.* **5**, Q09007. <https://doi.org/10.1029/2004GC000747>.

801 Gutmann, A., Bobrowski, N., Roberts, T.J., Rüdiger, J., Hoffmann, T., 2018. Advances
802 in bromine speciation in volcanic plumes. *Front. Earth Sci.* **6**, 213.

803 Halmer, M.M., Schmincke, H.U., Graf, H.F., 2002. The annual volcanic gas input into
804 the atmosphere, in particular into the stratosphere: a global dataset for the past 100
805 years. *J. Volcanol. Geotherm. Res.* **115**, 511–528.

806 Kutterolf, S., Hansteen, T.H., Appel, K., Freundt, A., Krüger, K., Pérez, W., Wehrmann,
807 H., 2013. Combined bromine and chlorine release from large explosive volcanic
808 eruptions: A threat to stratospheric ozone? *Geology* **41(6)**, 707-710.

809 Leroy, C.; Bureau, H., Sanloup, C., Raepsaet, C., Glazirin, K., Munsch, P., Harmand,
810 M., Prouteau, G., Khodja, H., 2019. Xenon and iodine behaviour in magmas. *Earth.*
811 *Planet. Sci. Lett.*, **522**, 144-154.

812 Louvel, M., Cadoux, A., Brooker, R.A., Proux, O., Hazemann, J-L., 2020a. New insights
813 on Br speciation in volcanic glasses and structural controls on halogen degassing. *Am.*
814 *Min.*, **105**, 795-802.

815 Louvel, M., Sanchez-Valle, C., Malfait, W.J., Pokrovski, G.S., Borca, C.N., Grolimund,
816 D., 2020b. Bromine speciation and partitioning in slab-derived aqueous fluids and
817 silicate melts and implications for halogen transfer in subduction zones. *Solid Earth*,
818 **11**, 1145-1161.

819 Mosbah, M., Clocchiatti, R., Michaud, V., Piccot, D., Chevallier, P., Legrand, F., Als
820 Nilsen, G., Grübel, G., 1995. Micro PIXE and micro SXRF: comparison of the two
821 methods and application to glass inclusions from Vulcano (Eolian Islands – Italy). *Nucl.*
822 *Instrum. Methods Phys. Res.* **B 104**, 481-488.

823 Munsch, P., Bureau, H., El Yakoubi, M., Khodja, H., Zaitsev, A., 2015. The use of ¹³C
824 diamond as pressure and temperature sensor for diamond-anvil-cell experiments. *Eur.*
825 *J. Mineral.* **27**, 365–375.

826 Newsom, H.E., 1995. Composition of the solar system, planets meteorites and major
827 terrestrial reservoirs. In: Ahrens, T.J. (Ed.), *Global Earth Physics*. American
828 Geophysical Union, Washington, DC, pp. 159–189.

829 Pichavant, M., Mysen, B.O., Macdonald, R., 2002. Source and H₂O content of high-
830 MgO magmas in island arc settings: an experimental study of a primitive calc-alkaline
831 basalt from St. Vincent, Lesser Antilles arc. *Geochim. Cosmochim. Acta* **66**, 2193–
832 2209.

833 Prescher, C., Prakapenka, V.B., 2015. DIOPTAS: a program for reduction of two-
834 dimensional X-ray diffraction data and data exploration. *High Press. Res.* **35(3)**, 223–
835 230.

836 Pyle, D.M., Mather, T.A., 2009. Halogens in igneous processes and their fluxes to the
837 atmosphere and oceans from volcanic activity: A review. *Chem. Geol.* **263**, 110-121.

838 Roberts, T.J., Vignelles, D., Liuzzo, M., Giudice, G., Aiuppa, A., Coltelli, M., Salerno, G.,
839 Chartier, M., Couté, B., Berthet, G., Lurton, T., Dulac, F., Renard, J.-B., 2018. The
840 primary volcanic aerosol emission from Mt Etna: Size-resolved particles with SO₂ and
841 role in plume reactive halogen chemistry. *Geochim. Cosmochim. Acta* **222**, 74-93.

842 Rocholl, A.B.E., Simon, K., Jochum, K.P., Gehann, R., Kramar, U., Luecke, W.,
843 Molzahn, M., Pernicka E., Seufert, M., Spettel, B. and Stummeier, J. (1997) Chemical
844 Characterization of NIST Silicate Glass Certified Reference Material SRM 610 by
845 ICPMS, TIMS, LIMS, SSMS, INAA, AAS and PIXE. *Geostand. Newslett.* **21-1**, 101–
846 114.

847 Rousseau, R.M., Detection Limit and estimate of uncertainty of analytical XRF results.
848 *Rigaku J.* **18(2)**, 33-47.

849 Shen, G., Wang, Y., Dewaele, A., Wu, C., Fratanduono, D.E., Eggert, J., Klotz, S.,
850 Dziubek, K.F., Loubeyre, P., Fat'yanov, O.V., Asimov, P.D., Mashimo, T.,
851 Wentzcovitch, R.M.M., 2020. Toward an international practical pressure scale: A
852 proposal for an IPPS ruby gauge (IPPS-Ruby2020). *High Press. Res.* **40(3)**, 299-314.

853 Shinohara, H., 2013. Volatile flux from subduction zone volcanoes: Insights from a
854 detailed evaluation of the fluxes from volcanoes in Japan. *J. Volcanol. Geotherm. Res.*
855 **268**, 46–63.

856 Sinnhuber, B.-M., Sheode, N., Sinnhuber, M., Chipperfield, M.P., Feng, W., 2009. The
857 contribution of anthropogenic bromine emissions to past stratospheric ozone trends: A
858 modelling study, *Atmos. Chem. Phys.*, **9 (8)**, 2863-2871.

859 Solé, A., Papillon, E., Cotte, M., Walter, Ph. and Susini, J., 2007. A multiplatform code
860 for the analysis of energy-dispersive X-ray fluorescence spectra. *Spectrochim. Acta*,
861 Part B **62**, 63–68.

862 Straub, S.M., Layne, G.D., 2003. The systematics of chlorine, fluorine and water in Izu
863 arc front volcanic rocks: implications for volatile recycling in subduction zones.
864 *Geochim. Cosmochim. Acta* **67**, 4179–4203.

865 Toby, B.H., Von Dreele, R.B., 2013. GSAS-II: the genesis of a modern open-source all
866 purpose crystallography software package. *Journal of Applied Crystallography*, **46(2)**,
867 544-549.

868 Urann, B.M., Le Roux, V., Jagoutz, O., Müntener, O., Behn, M.D., Chin, E.J., 2022.
869 High water content of arc magmas recorded in cumulates from subduction zone lower
870 crust. *Nat. Geosci.* **15**, 501-508.

871 Vidal, C.M., Métrich, N., Komorowski, J.-C., Pratomo, I., Michel, A., Kartadinata, N.,
872 Robert, V., Lavigne, F., 2016. The 1257 Samalas eruption (Lombok, Indonesia): the
873 single greatest stratospheric gas release of the Common Era. *Sci. Rep.* **6**:34868.

874 Wagner, W., Pruß, A., 2002. The IAPWS Formulation 1995 for the Thermodynamic
875 Properties of Ordinary Water Substance for General and Scientific Use. *J. Phys.*
876 *Chem. Ref. Data* **31**, 387.

877 Wallace, P.J., 2005. Volatiles in subduction zone magmas: concentrations and fluxes
878 based on melt inclusion and volcanic gas data. *J. Vol. Geo. Res.* **140**, 217-240.

879 Webster, J.D., de Vivo, B., 2002. Experimental and modeled solubilities of chlorine in
880 aluminosilicate melts, consequences of magma evolution, and implications for
881 exsolution of hydrous chloride melt at Mt. Somma–Vesuvius. *Am. Mineral.* **87**, 1046–
882 1061.

883 Webster, J.D., Holloway, J.R., Hervig, R.L., 1989. Partitioning of lithophile elements
884 between H₂O and H₂O+ CO₂ fluids and topaz rhyolite melt. *Econ. Geol.* **84**, 116–134.

885 Webster, J.D., Kinzler, R.J. Mathez, E.A., 1999. Chloride and water solubility in basalt
886 and andesite melts and implications for magmatic degassing. *Geochim. Cosmochim.*
887 *Acta* **63**, 729–738.

888 Webster, J.D., Baker, D.R., Aiuppa, A., 2018. Halogens in Mafic and Intermediate-Silica
889 Content Magmas. In: Harlov, D., Aranovich, L. (eds) *The Role of Halogens in*
890 *Terrestrial and Extraterrestrial Geochemical Processes*. Springer Geochemistry.
891 Springer, Cham.

892 Witt, M.L.I., Mather, T.A., Pyle, D.M., Aiuppa, A., Bagnato, E. & Tsanev, V.I., 2008.
893 Mercury and halogen emissions from Masaya and Telica volcanoes, Nicaragua. *J.*
894 *Geophys. Res.* **113**, B06203.

Experiment-Run	Pressure (GPa)	Heating cycle	Laser Temperature °C	Pressure medium/fluid	Bromine concentration (µg/g)			D ^{Br} _{fluid/melt}
					melt	glass	fluid	
<i>hydrous experiments</i>								
Cpo2	< 1.1	0	RT	water		11160 ^a	48 ^a	
	< 1.1		RT	water			26 ^a	
	< 1.1	1 ^b	nd ^g	water		1070	2029	1.9
LN22	< 1.1	0	RT	water		11120 ^a	18 ^a	
	< 1.1	1 ^b	nd ^g	water		2739	7455	2.72
	< 1.1	2 ^b	nd ^g	water		3267	6864	2.10
	< 1.1	3 ^b	nd ^g	water		2124	7027	3.31
	0.4 ^f	4 ^b	nd ^g	water		3282	7178	2.19
Cpo3	< 1.1	0	RT	water		12440 ^a	79 ^a	
	< 1.1		nd ^g	water			2563	
	< 1.1	1 ^b	nd ^g	water			2130	
	< 1.1		nd ^g	water			2498	
	< 1.1		RT	water		1990	2370	1.19
LN11	< 1.1	0	RT	water		12610 ^a	-/80 ^{a,d}	
	< 1.1	1	nd ^g	water		12410	3462/358 ^d	0.28/0.03 ^e
	< 1.1	2	nd ^g	water		1062	4161/326 ^d	3.92/0.31 ^e
	< 1.1	3	nd ^g	water		1438	4783/267 ^d	3.33/0.19 ^e
	< 1.1	4	nd ^g	water		1752	5784/226 ^d	3.30/0.13 ^e
	0.53 ^f	5	nd ^g	water		1545	5337/565 ^d	3.45/0.37 ^e
<i>neon experiments</i>								
Mar1	1.7	0	RT	Neon		10620 ^a	209 ^a	
	1.7	1	1875	Neon	14640			
	1.7		1810	Neon	15350			

	1.7		≈ 1800	Neon	15200			
	1.7		≈ 1800	Neon	14720			
	1.7		≈ 1800	Neon	16430			
	1.7		RT	Neon		16760	6212	0.37
Hak1	1.1	0	RT	Neon		10019 ^a	1062 ^a	
			2005	Neon	32046			
		1	2120	Neon	45065			
	1.1		RT	Neon		11019	4153	0.38
			nd	Neon	43095			
		2	2167	Neon	11256			
	1.1		RT	Neon		10148	3985	0.39
			2057	Neon	10623			
		3	2057	Neon	9864			
	< 1.1		RT	Neon		10128	208	0.02
Hak2	≥ 1.4	0	RT	Neon ^c		10138 ^a	11760 ^a	1.16
	≥ 1.4	1	≈ 1725	Neon ^c		4333	7087	1.64
	≥ 1.4	2	≈ 1725	Neon ^c		4398	8060	1.83
	1.4	3	≈ 1725	Neon ^c		5974	10314	1.73

897

- ^a Initial bromine concentration measurements were done in a compressed cell at ambient temperature before the first heating.
- ^b External heating kept the temperature at 235-265 °C when the las was shut off to enable fluid circulation.
- ^c The Neon fluid became enriched in water that was first released from the basalt glass in run Hak1-3 and together recompressed for Hak2 runs.
- ^d Two separate fluid analyses were conducted: '*next to the melted glass*'/'200 μm away from the glass'.
- ^e Partition coefficients calculated for the fluid '*next to the melted glass*'/'200 μm away from the glass'.
- ^f Determined by ice-water transition from Nitrogen cooling after the experiment.
- ^g Laser temperature was above the liquidus temperature for hydrous basalt (> 1300 °C). The absence of crystals was monitored with SXRD.

898

899 Table 1 Experimental runs. Bromine was analyzed with synchrotron x-ray fluorescence. Uncertainties on the
900 bromine concentrations are of 10% relative. RT = room temperature; nd = not detectable. The volume of the fluid fraction
901 was estimated from sense of proportion and ranges from 25 to 45 wt.%.

Experiment-Run	Heating cycle	Pressure		
		water-ice VI transition	ruby	gold
Cpo2	0	< 1.1 ^a		2.6 ^b
	1	-		2.1
LN22	0	< 1.1 ^a		2.1 ^b
	1	-		-
	2	-		-
	3	-		-
	4	0.4 ^c		2.0 ^c
Cpo3	0	< 1.1 ^b		1.6 ^b
		-		-
	1	-		-
		-		-
		< 1.1		2.1
LN11	0	< 1.1 ^b		1.9 ^b
	1	< 1.1		-
	2	< 1.1		0.8
	3	< 1.1		0.9
	4	< 1.1		1.2
	5	0.53		2.0
Mar1	0		1.7 ^{b,c}	2.7 ^{b,c}
			1.7	-
			1.7	-
	1		1.7	-
			1.7	-
			1.7 ^c	3.2 ^c
Hak1	0		1.1 ^{b,c}	3.3 ^{b,c,d}
	1		1.1	-
	2		1.1	-
	3		< 1.1	3.1 ^d
Hak2	0		1.4 ^b	-
	1		≥ 1.4	2.8
	2		≥ 1.4	2.4
	3		1.4 ^c	1.9 ^c

- a Water-ice transition measurements were conducted after the experiment and after the cell cooled down to room temperature.
- b Initial pressure measurements were done in a compressed cell at ambient temperature before the first heating.
- c Pressure values are used for the method correlation in Figure 2.
- d Diffraction peaks could be also neon at 1.2 GPa.

903

904 Table 2 Experimental pressures calculated from the equation of state (EOS) of
 905 water-ice VI transition, ruby fluorescence, and EOS of gold.

906

SiO ₂	44.9(2)
TiO ₂	1.08(3)
Al ₂ O ₃	14.5(1)
Cr ₂ O ₃	0.09(2)
FeO	8.45(7)
MnO	0.15(2)
NiO	0.03(2)
MgO	11.8(1)
CaO	10.66(6)
Na ₂ O	2.61(6)
K ₂ O	0.50(1)
P ₂ O ₅	0.10(2)
Total	95.6(3)

907

908 Table 3 Major and minor element composition of the basaltic glass stating material
 909 measured with electron microprobe analysis. Uncertainties (1 s.d.) are given in
 910 parentheses showing the first significant digit.

911

Sample	Bromine ($\mu\text{g/g}$)
BaM024	10812
Cpo2-0	11160

LN22-0	11120
Cpo3-0	12440
LN11-0	12610
Mar1-0	10620
Hak1-0	10019
Mean	11254
SD	726

912

913 Table 4 Bromine concentration in the starting glass measured by synchrotron x-ray
 914 fluorescence and electron microprobe analysis. Uncertainties on the bromine
 915 concentrations are of 10% relative.

HBr (Gg/year)		Study
<i>volcanic flux</i>		
based on SO ₂ flux from the respective study	with SO ₂ flux from Carn et al. (2017)	
2.6-43.2	-	Halmer et al. (2002)
13		21.4 Aiuppa et al. (2005) Pyle and Mather (2009)
5-15		8-23 Webster et al. (2018)
10.5		14.4 Cadoux et al. (2022)
9		12.3
<i>melt inclusions</i>		
23.5-72.9		this study

916

917 Table 5 Estimates of annual global volcanic bromine flux to the atmosphere.

918